Measurement of the angular distributions of particles in air showers

S. Gamp, D. Brecht, W. Hofmann, T. Kihm, J. Knöppler, V. Matheis,
M. Panter, R. Reimers, M. Rosales,* C. A. Wiedner, H. Wirth, and R. Zink
Max Planck Institut für Kernphysik, D-6900 Heidelberg 1, Germany

J. Heintze, P. Lennert, and S. Polenz
Physikalisches Institut der Universität Heidelberg, D-6900 Heidelberg 1, Germany
(Received 13 April 1992)

Using a scintillator air shower array to determine the direction, size, and core position of extensive air showers and a large-volume drift chamber to track individual shower particles, we have measured the angular distributions of charged particles in extensive air showers at sea level. The distributions are sharply peaked around the shower axis, with characteristic widths of a few degrees. Particles at large distances from the shower axis tend to point towards the axis as their origin. Monte Carlo models of air showers reproduce the measured distributions rather well.

PACS number(s): 96.40.Pq

I. INTRODUCTION

The observation by the Kiel group of an excess of high-energy extensive air showers from the direction of Cygnus X-3 [1] has triggered an enormous interest and a revival of this field of cosmic ray physics. If those observations, and in particular the unusual properties of the presumed γ-ray showers from Cygnus were confirmed, the impact on both astrophysics and particle physics would be considerable. Several large air shower arrays were constructed or enlarged to search for point sources emitting in the PeV energy range; most of these arrays use conventional scintillation counters, and derive the arrival direction of the shower plane from timing measurements. At lower energies, and higher fluxes, imaging Cherenkov telescopes are used to detect the Cherenkov light from air showers. With this technique, the Whipple group succeeded to establish beyond any doubt the Crab nebula as a source of TeV γ rays [2]. Both techniques have disadvantages: Cherenkov telescopes have a very limited field of view and a rather low duty cycle; scintillator arrays require a large lever arm on the ground to determine the shower direction from the arrival times, and fail for small, localized showers. As a consequence, one is looking for alternative techniques that combine the duty cycle of air shower arrays with a good angular resolution even at TeV energies, and which allow to cover the energy range between imaging Cherenkov telescopes and conventional arrays. Candidate technologies include water Cherenkov counters [3,4], nonimaging [5] as well as solar-blind Cherenkov counters [6], and tracking detectors to follow individual shower tracks [7,8].

The basic idea behind the tracking technique is to exploit that secondary tracks in a photon-initiated shower tend to follow the direction of the primary, and can be used to point back to the source even for rather small showers, provided that a minimum number of tracks are detected. As detailed in the initial proposal for the Cosmic Ray Tracking (CRT) project [8], an array of tracking detectors could give an angular resolution of 0.3° down to its threshold in the TeV range. The CRT detectors, 384 in total, track charged particles over an area of about 2.5 m^2 per module, and allow an efficient muon identification on a track-by-track basis, which is important for the rejection of hadronic showers.

The CRT principle rests on the fact that the angular distribution of tracks in an air shower is sharply peaked around the direction of its primary. While the processes in the development of air showers are reasonably well understood and are implemented in several Monte Carlo programs, it seemed nevertheless very important to obtain real data on these fundamental distributions. For this purpose, a half-scale prototype of a tracking detector as proposed in [8] was operated in coincidence with a small scintillator air shower array constructed for this purpose (Fig. 1). The air shower array measures the global shower parameters such as core position, direction, and shower size; the CRT module is then used to study individual shower tracks. In this paper, we report on first measurements of angular distributions of charged particles in showers. Studies on related topics, such as the distribution of muons or the reconstruction of the shower axis using the detected tracks, are in progress and will be reported at a later date.

In the following sections, we will discuss the construction and performance of the CRT prototype module (Sec.

*On leave from Universidad de los Andes, Merida, Venezuela.

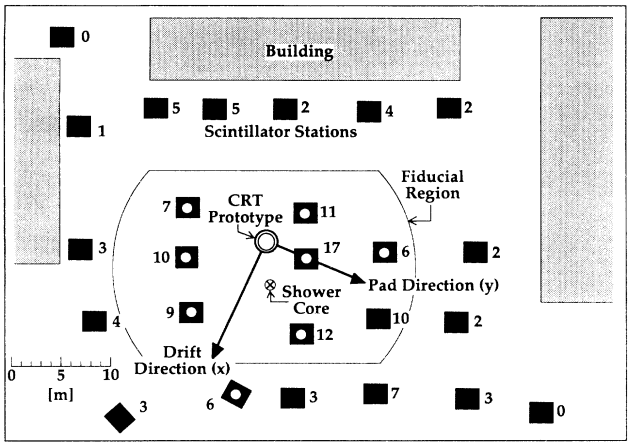

FIG. 1. Air shower array operated at the Max Planck Institut für Kernphysik. The 25 stations contain scintillators with 0.8 m^2 active area. The stations marked with a white dot provide the trigger for the array. Shower cores are accepted within the indicated fiducial region. The numbers show the pulse heights (in units of particles) for a typical shower with its core indicated near the center of the array. Also shown is the location of the half-scale CRT prototype module, and the orientation of the drift chambers inside the module.

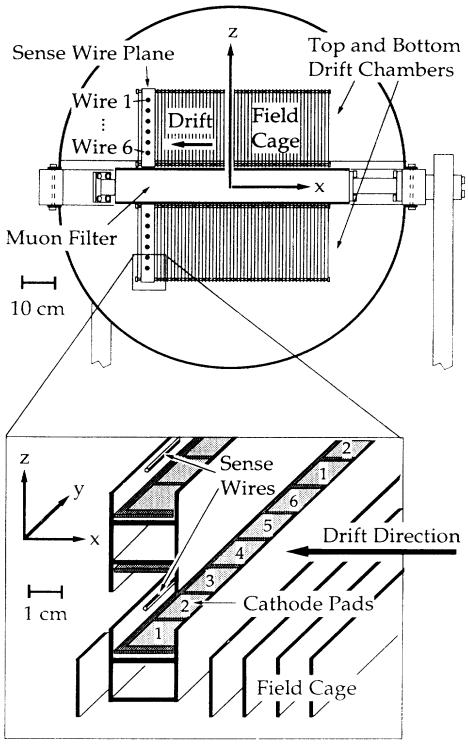

FIG. 2. Illustration of the half-scale prototype module, showing the two drift chambers with their field cages and sense wire planes, the iron muon filter, and the vessel consisting of the aluminum support ring and two aluminum half-spheres. The support ring also contains all feedthroughs for supply voltages and signal cables. The lower figure gives details of the construction of the wire chamber, where aluminum profiles are used to define the gas amplification cells. Printed circuit boards in the profiles provide the cathode pads for the determination of the coordinate along the wire. The pads are read out through traces on the back of the board; every sixth pad in a row is connected to the same electronics channel.

II), the layout and properties of the scintillator air shower array (Sec. III), and the measurement of particle distributions in showers (Sec. IV).

II. THE HALF-SCALE CRT PROTOTYPE MODULE

Shortly after the first discussion of the CRT project, the construction of a half-scale prototype CRT module was started to demonstrate the feasibility of the device, to explore alternatives for various design details, to test the readout electronics and to develop the necessary on-line software, to investigate various effects that could deteriorate the resolution, and finally to make first measurements of particle distribution in air showers.

The half-scale prototype shares many of its basic features with the full-size modules [8,9]. It contains two large-volume ($60\times61\times24$ cm^3) drift chambers separated by a 10 cm iron plate (Fig. 2) which serves as a muon filter. The upper and lower chambers are mounted on the iron plate, which in turn is mounted in a 1.34 m diameter aluminum support ring. Two hemispherical aluminum shells of 1.24 m diameter complete the vessel. The thickness of the aluminum half-spheres is about 3 mm. In the following, we will often refer to the local (right-handed) module coordinate system, where the x axis is along the drift direction, the z axis is upwards, and the y axis points along the wires.

A. Drift chambers

The drift chambers each consist of a field defining structure ("field cage") to maintain a uniform drift field over the active region, and a six-wire proportional chamber to detect the electrons from ionization. For an ionizing particle crossing the drift region, up to six space points are recorded. Their coordinates are defined by the wire position (z), by the drift time (x), and by the signals induced on cathode electrodes along the wires (y). The drift chamber signals are read out by a 100 MHz flash analogue-to-digital converter (ADC) system.

The purpose of the field cages is to generate a uniform electric field over the entire sensitive volume. In contrast to the final design with field cages made of printed circuit boards, we used in this prototype a series of 2 mm thick brass frames, spaced at 1 cm, which are connected to a voltage divider chain (Fig. 2). This construction implies a non-negligible amount of material in front of the active volume, namely 4.5 g/cm^2 or 0.32 radiation lengths, on average. The chamber was operated with an argon/methane 80%/20% gas mixture and a drift voltage of 18.3 kV, corresponding to a drift field of 300 V/cm, a drift velocity in the plateau region around 7 $cm/\mu s$, and a maximum drift time of about 9 μs.

The field cage is terminated by a proportional chamber for charge collection; the chamber consists of six sense wires running horizontally, spaced at $d=4$ cm and separated by aluminum profiles, which serve to define the electric field near the sense wires, to limit the entrance window for each wire, and to carry a printed circuit board with cathode segments ("pads") (Fig. 2). The wires are usually biased at 1725 volts, corresponding to a (visible) gas gain of 4.2×10^4. The coordinate along a sense wire is determined from the charges induced on the cathode pads underneath and above each wire. Each pad is $w=12.6$ mm (along the wire) by $h=16.4$ mm (perpendicular to the wire). To limit the number of readout electronics channels, every sixth pad is connected to the same preamplifier and readout channel, through readout lines on the back of the board. Coordinates along each wire (y) are determined from these six signals; in most cases, at least three adjacent pads will exhibit signals above the noise level (Fig. 3). The multiplexing of the pads causes an ambiguity; coordinates are measured up to multiples of the length of the pad period $L=6w=77$ mm. Consider now the angle β, defined as the angle between the projection of a track onto the wire plane and the z (up) axis. Two tracks with slopes $\tan\beta_1$ and $\tan\beta_2=\tan\beta_1+nL/d$ (with integer n) will result in identical pad signals and cannot be distinguished. In the reconstruction software, all tracks are therefore mapped into the interval $-L/2d<\tan\beta\le L/2d$, or $-44°<\beta\le44°$. This ambiguity is of little relevance both for the application in an extensive air shower (EAS) array and for the measurements described in the following, since a typical EAS array effectively triggers on showers within about 30° from the zenith, and since the majority of the tracks closely follow the direction of the primary.

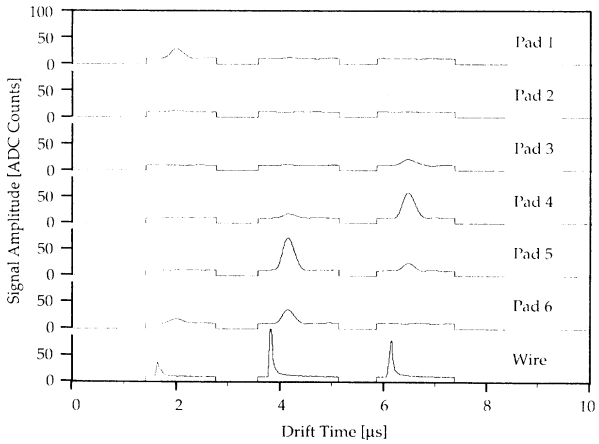

FIG. 3. Typical signals of a sense wire and of the associated six cathode pads, after digitization through the flash ADC. With the drift velocity of about 7 cm/μs, the maximum drift distance of 60 cm corresponds to a maximum drift time of about 9 μs. In this example, the first hit is located between pads 1 and 6, the second close to pad 5, the third close to pad 4. The breaks in the baseline between signals are caused by the readout algorithm: the readout processor first scans the data for hit candidates and then transfers only data in certain time intervals around the hits.

The sense wires are connected to Fujitsu MB-43468 preamplifiers with about 10 ns rise time. Since the cathode pads represent a current source with a large source capacitance C, a significantly longer shaping time was used for the pads to reduce electronics noise (which in this regime is proportional to $C/\sqrt{\tau}$). The pads were connected to a standard time projection chamber (TPC) amplifier chain [10] with charge sensitive preamplifiers and shaping amplifiers, with a combined rise time of about 100 ns. The preamplifiers were modified to reduce the input impedance and to speed up the charge collection. Typical noise values were 7000 e rms for the wire signals, and 10 000 e rms for the pad signals.

The analog-to-digital conversion was performed by 100 MHz VME wave form recorders (Struck DL 400); for a few channels in the lower drift chamber 60 MHz modules (Le Croy 2262) were used, because of lack of DL400 channels. The DL400 modules provide a depth of 1024 samples at 8 bit resolution; the LC2262 has 632 samples and a nominal resolution of 10 bit. The readout of the VME crate was controlled by a local 68020 CPU, which transferred the data through a buffer memory in the CAMAC crate to the main on-line computer, a VAXSTATION 3200. The trigger for the readout was derived from the scintillator array, although the CRT module could also be operated in a self-triggered mode, with rates around 60 Hz for a three-wire coincidence trigger. This rate is consistent with cosmic ray rate over the area of the chamber.

On-line calibration was provided at several levels. Before a run, the digital-to-analog-converter (DAC) controlled pedestals of the ADCs were preset to a nominal value, and in case of the charge-coupled device (CCD) modules the change of the pedestals between early and late samples ("droop") was adjusted to zero. During each run, a pedestal event with a random trigger was interleaved after 100 real events, and 50 events with test pulse signals on pad and wire channels were taken every 30 min. The drift velocity was continually monitored using the distribution of drift times for reconstructed hits.

To investigate systematic distortions caused for example by irregularities in the field cage, by space charge effects, or by wrong boundary conditions at the transition from the field cage to the wire plane, the module was equipped with a laser calibration system generating several remotely controlled beams and was extensively tested before the cosmic ray run. In these tests, systematic distortions were demonstrated to be small compared to the resolution of the chambers.

B. Data analysis

A typical event is shown in Fig. 4, where the digitized wire current is shown as a function of drift time. In this rather busy event, the module was located near the core of the shower. The analysis procedure involves first a hit finding step, followed by a pattern recognition and track fitting step. The hit finding is based on a "difference of samples" (DOS) technique, where first the differences between adjacent samples are formed, and where a hit is

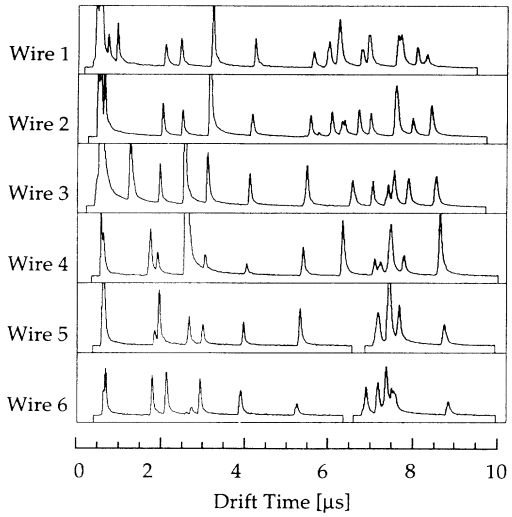

FIG. 4. Typical event in the CRT prototype module, showing the signals on the six sense wires of the upper drift chamber as a function of time, after digitization with the flash ADC. See Fig. 3 for additional remarks.

defined as three successive difference values above a certain threshold. Once a signal is found in a wire electronics channel, the charges on the corresponding cathode pads are integrated over a time window determined by the timing and length of the wire pulse. Since the pad readout channels have a longer shaping time than the wire channels, the pad integration window is shifted compared to the wire signal (Fig. 3). In the wire data, double hits are resolved for hit separations of $>6-8$ mm; a larger hit separation is required for the pad data. The pattern recognition is primarily based on wire signals and searches for straight tracks. Tracks are found by looping over all hits on two "seed wires," and scanning the other wires for hit candidates in a 3 mm window around the line defined by the two hits on the seed wires. A minimum of five hits is required; at this first stage hits may be shared with another track. In a cleaning step, track candidates with multiple shared hits are successively eliminated, until only tracks with at most one shared hit are left. The individual hits are assigned errors based on the track angle and the drift distance (see below), and a track fit is performed. Only tracks with a fit probability exceeding 2% are accepted. The hit positions along the wires are obtained by a Gaussian fit to the charges of the pad with the maximum pulse height, and of its two neighbors. For tracks found in the wire data, a line fit is performed for the cathode pad positions. Because of their longer shaping times, the pad signals are prone to multitrack overlap problems. Since many results on track distributions can be obtained using only the drift (x-z) view, tracks with poor pad fits were kept, and cuts on the quality of the pad fit were applied only if these data were actually used in the analysis. (Future full-scale modules will use the identical short shaping times for both pad and wire signals.)

C. Performance

The resulting resolution both in the drift direction (x) and in the wire, or cathode pad, direction (y) are shown in Fig. 5, both as a function of the drift distance and as a function of the track angle α. Here, α is defined as the angle between the z ($=$ up) axis and the projection of the track onto the x-z plane in case of the drift coordinate measurement, and onto the y-z plane in case of the cathode pad coordinate. $\alpha=0$ means that the track segment "seen" by the wire is perpendicular to the direction of the measurement. The stochastic distribution of ionization events along the track can cause deviations between the center of gravity of the charge deposition and the middle of the track segment, resulting in measurement errors increasing with α [11].

The resolutions given in Fig. 5 were derived from the fit residuals, multiplied by the appropriate correction factors depending on the number and spacing of the points used in the fit. Within margins small compared to the resolution of the chamber, all residuals were centered at zero, indicating that systematic distortions can be neglected. The tracking errors increase with increasing drift distance due to diffusion, and with increasing track angle due to ionization fluctuations. The resulting average error in the track direction, derived from the individual measurement errors, is about 4 mrad for the track slope in the x-z projection, and about 6 mrad in the y-z projection.

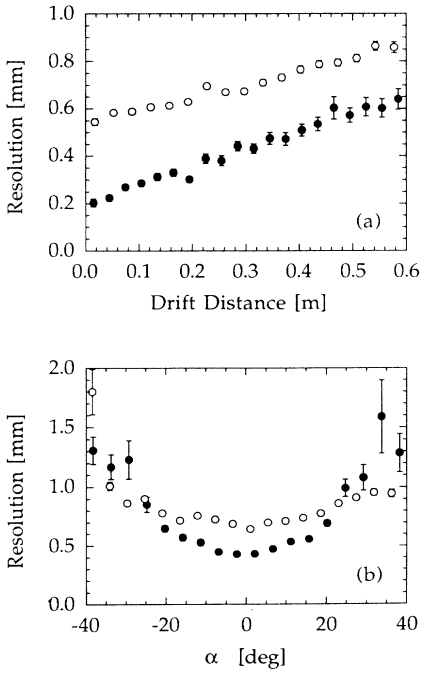

FIG. 5. Position resolution in the drift direction (solid circles) and in the direction along the wires (open circles), as a function of the drift distance for small-angle tracks (a), and as a function of the track angle with respect to the measurement direction, for tracks at medium drift distances (b).

D. Monte Carlo simulation

Various Monte Carlo codes were used in the optimization of the module layout and in the tuning of the analysis software. Tracking of shower particles in the CRT module is handled by GEANT [12]. Special codes simulate ionization energy loss at the level of individual electrons and clusters, followed by transport and diffusion in the (numerically modeled) electric field, gas amplification (with individual gain factors following a Polya distribution), signal amplification, shaping and digitization. Because of the CPU requirements of such a detailed simulation, the "standard" version of the simulation program simply smeared the GEANT-generated hits with resolution functions depending on the deposited charge, the drift distance, the track direction, and the proximity of other tracks.

III. THE EAS TRIGGER ARRAY

A. Layout

To select extensive air showers and to measure their core position, direction, and size, we installed a small air shower array consisting of 25 scintillator stations distributed over an area of 50×40 m^2. The spacing of 6 to 10 m between detector stations was chosen to optimize the determination of the core position, given a fixed number of stations. Since the array had to fit between existing buildings and roads, the layout does not exactly follow a square grid (see Fig. 1). Each scintillator station contains two square scintillation counters of 0.8 m^2 area, positioned on top of each other. The scintillators, 1 cm thick material (SCSN38), are read out with wavelength shifters along two edges, which are in turn coupled to EMI 9954 photomultipliers (PM's). The scintillators are partly masked with tape to provide a homogeneous response within 10% rms over the whole area. The scintillation counters, which were previously used in a hadron calorimeter, are not optimized for timing measurements, given the position-dependent propagation delays and the relatively slow fluorescent readout. To partly overcome this deficiency, the two scintillators of each station are oriented with the readout on opposite sides (Fig. 6); the earliest signal determines the timing of a station. Each station is housed in a simple sheet-metal shed; the PM's are connected with RG58 coaxial cables to the readout electronics located in a trailer near the center of the array. Each PM signal is split and is fed into a discriminator (Le Croy 4413 or 4416 B) and then into a 10 bit time-to-digital converter (TDC) with 0.25 ns resolution (Le Croy 2228 A). The discriminator thresholds correspond to about 10% of the single-particle amplitude. The other split analog signal is digitized with an 11 bit ADC (Le Croy 2249 W). The start signal for the TDC's and the gates for the ADC's are derived from the array trigger coincidence; the individual PM signals are delayed to provide the TDC stops. The trigger for the array is derived from the eight stations close to the center of the array (see Fig. 1). Their 16 PM signals are combined in a majority coincidence with an adjustable trigger threshold. The ADC's and TDC's as well as various *I/O* registers and test pulse generators are controlled by the VAX 3200 through CAMAC; the system is capable of operating at trigger rates of up to 200 Hz. With the standard trigger condition of 8 out of the 16 scintillators, the typical rate is much lower, about 0.5 Hz.

FIG. 6. Construction of a scintillator station, showing the two scintillator plates with the readout by wavelength shifter bars on two sides.

B. Calibration

For the analysis of the scintillator data, various calibration constants are needed, such as the positions of the stations as well as the offsets and conversion coefficients of both the TDC's and ADC's. The positions of the stations were surveyed with a precision of a few cm. An automatic calibration procedure for the ADC's and TDC's is run once per hour, consisting of 50 randomly triggered events to measure ADC pedestals, of 300 test pulses from a precision timing generator to derive TDC slopes, and of 50 events each to calibrate propagation and cable delays. This is achieved by injecting, at the position of the signal splitters, a current pulse into the cables to the scintillator stations. Depending on the timing of the global trigger with respect to the timing of the current pulse, one can use this pulse to calibrate either the propagation time from the signal splitters through the discriminators to the TDC's, or the time for propagation back to the PM, where the signal is reflected, returned to the central electronics, and propagated to the TDC's. From these two measurements, the temperature-dependent signal speed in the RG58 cables can be determined and corrected for; indeed, shifts by as much as 1.5 ns were measured between day and night. All these measurements are summarized in calibration files; stations with calibration constants outside a preset range are automatically disabled in the further analysis. The relative timing of the stations is checked on a weekly basis by moving a test counter with fixed cable length from station to station, resulting in one additional calibration constant per TDC channel. A five-minute run per station was sufficient to achieve 0.2 ns accuracy for this correction. This additional timing correction was constant within typically ± 0.5 ns.

The high voltages for all PM's are adjusted to provide a dynamic range of at least 40 minimum ionizing particles. Precise values for the conversion coefficients of the ADC's, that is, the number of ADC channels per minimum ionizing particle, are derived from the peak position in the pulse height spectra (Fig. 7); after a coarse determination of the peak position, a parabola is fit near the peak. To suppress events with more than one hit per

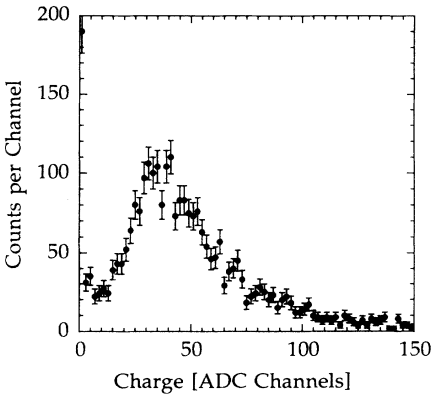

FIG. 7. Distribution of signals for one scintillator, requiring a signal consistent with a single particle in the second scintillator of the station.

scintillator, the calibration spectra for one counter are accumulated under the condition that the second counter of the station has a pulse height consistent with a single particle. The conversion coefficients are determined separately for each 24-h run.

C. Data analysis and cuts

During normal operation, the array raw data as well as the calibration events are saved to storage media. Off line, a data summary file is created, containing the raw data, the calibration records, and the calibrated scintillator information. At this stage, further cross checks on the reliability and consistency of the data are performed. For example, the timing and amplitude measurements of the two scintillators in a station are required to agree within 2 standard deviations (s.d.). A combined timing signal is defined by the earlier of the two times. The smaller of the two signals is used for amplitude, to minimize the effect of Landau fluctuations. Time slewing corrections are applied, and appropriate timing and amplitude errors are assigned. Events with signals in less than 10 scintillator stations are rejected. At this stage, we obtain a single-particle timing resolution of about 3.1 ± 0.3 ns for the earlier of the two signals, averaged over the area of the counters, compared to 4.2 ± 0.2 ns for a single scintillator. Figure 1 lists the pulse heights for an event with its shower core near the center of the array.

In the next analysis step, shower shapes are fit to the scintillator data, and the results are added to the data summary file. Options range from analytical fits of a simple plane wave front with three parameters, two variables to describe the shower direction and the arrival time, to iterative seven-parameter fits of a cone-shaped shower front described by the direction, the arrival time, the opening angle of the shower cone, the position of the shower core, and the shower size. For the iterative fit, shower directions of the simple plane fit are used as starting values; multiple starting values for the core position are tried to avoid trapping in a local minimum. To describe the radial dependence of particle density in a shower, we use a variant of the modified Nishimura-Kamata-Greisen (NKG) distribution [13]

$$\rho(r)=\frac{0.44N}{r_0^2}\left[\frac{r_0}{r_c+r}\right]^{2-s}\left[\frac{r_0}{r_0+r}\right]^{4.5-s}\left[1+\frac{r}{11.4r_0}\right]$$

with a fixed shower age $s=1.25$. N is the shower size, and $r_0=79$ m is the Moliere radius. Compared to the standard form given in the literature, we introduce an additional cutoff parameter $r_c=2.6$ m to smooth the behavior at short distances from the core. For most applications, we use a six-parameter cone fit where the slope of the shower front is fixed to 0.04, in agreement with measurements by other EAS arrays, and with Monte Carlo simulations. The fitting procedure eliminates stations with timing or amplitude values more than 3 s.d. from the fit, provided that the majority of the stations in the event is acceptable, and cuts on the quality of the fit are applied.

In their initial implementations, all fits were based on χ^2 minimization. A problem with this type of fit is that the response function of scintillators to single particles is highly non-Gaussian due to Landau and path length fluctuations resulting in an asymmetric distribution (Fig. 7). In our calibration procedure, the charge corresponding to one minimum ionizing particle is defined as the maximum of the single-particle energy loss distribution. However, if many particles hit a scintillator, the most likely signal is essentially m times the *mean* signal per particle, rather than m times the *most likely* signal. The minimum-χ^2 fit, which is based on the assumption of Gaussian measurement errors, did introduce a systematic, size-dependent bias in the determination of the shower size. Particularly critical are small showers, where scintillators with single-particle hits combine with a few stations with larger pulse heights. As a remedy, a maximum likelihood fit was implemented; the expected distribution for m shower particles hitting a particular detector is obtained by convoluting m times the single-particle response function, which is measured as part of the normal calibration procedure. The probability distribution for a scintillator hit by a shower is obtained by averaging these many-particle response functions with weighting factors corresponding to a Poisson distribution with its mean given by the NKG shape. When tested with Monte Carlo events, this fit did improve the fit errors on the shower size slightly, and did remove the bias. For other fit parameters, such as the core position, the improvement was only marginal.

To ensure proper convergence of the fits, and to select only events where both the core position and the shower direction are reasonably well determined, we require that the station with the largest signal shows at least 3 minimum ionizing particles, but not more than 30 particles (to avoid saturation), and is not located on the border of the array. Furthermore, we reject events with a core distance of more than 10–15 m from the center of the array (see Fig. 1 for the definition of the fiducial region), and with shower sizes of less than 30 000 charged particles; without these cuts, the quality of the reconstruction of shower parameters is insufficient, mainly due to

difficulties in locating the shower core. Only showers within 30° from the zenith are used. Figure 8 shows the resulting spectrum of shower sizes. (The cut at $30k$ shower size is not a sharp edge, since the cut is effectively applied twice, first after the χ^2 fit and then after the likelihood fit, where shower sizes are recalculated.)

D. Resolution

For events passing the selection cuts, the uncertainties on the fit parameters, such as the shower direction and the core location, are mainly a function of the shower size N. Figure 9 displays the mean errors as given by the covariance matrix of the fit as a function of N; the array provides a typical precision of about 1° to 1.5° on the direction of the shower axis, and of 1 to 2.5 m on the core location in x or y. The shower size is typically determined within 15–20 % rms. One method to check that these errors are realistic is the "chess board" technique, where the array is subdivided into two sub-arrays, which are analyzed independently. Assuming that the sub-arrays provide independent measurements of the shower direction (which is, according to the Monte Carlo simulation, a valid assumption for our configuration), and given that the angular errors on the two sub-array fits are similar, the width of the difference distribution of the two measurements is $\sqrt{2}$ times the individual resolution, and the width of the average (corresponding to the combined global fit) is $1/\sqrt{2}$ times the individual resolution, or $\frac{1}{2}$ times the width of the difference distribution. The resolutions obtained this way are included in Fig. 9. In the determination of the core position, the sub-array comparison suffers from the fact that the two measurement errors are frequently quite different; therefore we used only those events in the comparison, where the measurement errors agreed within 20%. Another way to check the reliability of the error estimates is of course to compare in Monte Carlo events the true and the reconstructed parameters (Fig. 9). We see that the fitting procedure tends to underestimate the true errors slightly, which is not surprising, given that in particular in the determination of the core position, the log(likelihood) function has a very complicated structure, where a parabolic approximation near the minimum has only limited validity.

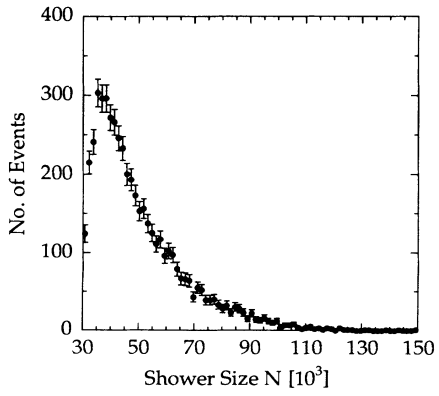

FIG. 8. Spectrum of shower sizes after the event selection cuts described in the text.

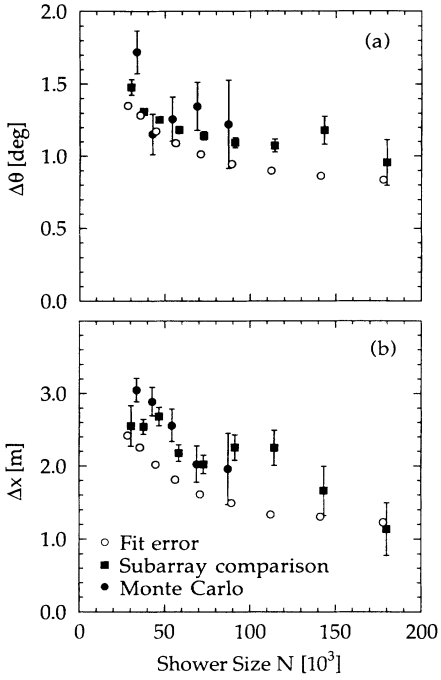

FIG. 9. Experimental resolution in the determination of the shower direction (projected onto the x-z plane) (a) and of the core location (b). Shown are the errors quoted by the fitting procedure (open circles) as well as the result obtained by comparing the two shower directions from a chessboard fit (squares, see text). Also included is the rms difference between true and reconstructed shower parameters of Monte Carlo events (solid circles).

E. Systematic errors

Two types of systematic errors merit discussion here: errors in the determination of the shower size, and a systematic bias in the determination of the shower axis. Concerning the determination of the size, we note that the array samples particle distributions only to distances of about 20 m from the core, corresponding to about 20% of all shower particles. The extrapolation to the full size relies entirely on the assumption concerning the radial distribution function. The modified NKG expression given above describes Monte Carlo data well, but it cannot be verified in this experiment. Together with uncertainties in the shape of the scintillator response, we estimate a 40% systematic scale uncertainty in the measurement of shower sizes.

Particularly dangerous for the measurement of angular distributions is any position-dependent bias in the determination of the shower axis. A wrong assumption concerning the slope of the shower front might for example cause all showers near the periphery of the array to appear tilted towards the array center. Various techniques were used to search for such systematic errors. One

method is to determine the average direction of showers as a function of core location. Since (for a planar array) the acceptance should not change if the shower axis rotated 180° around the vertical, one expects the "average shower" to point exactly upward, everywhere in the array. We found a maximum deviation of 0.5°, different from zero by only two standard deviations. In the chess board fits, systematic deviations between the two subarrays were at most 0.4°. Another test was to use showers with a core near the center of the array, and to refit their direction using only information from the right or left half of the array. Any bias due to edge effects would cause a systematic shift between the full fit and the fit using only the right or left half-array. Again, no systematic effects exceeding 0.5° were observed. In summary, we consider 0.5° as an upper limit for systematic errors in the determination of the shower axis.

F. Monte Carlo simulation

In the simulation of the array and its performance, we use the CORSIKA [14] and AIRCAS [15] codes to generate showers in the energy range of a few 10^{14} eV, both for protons and heavier primaries. A simplified model is used to approximate propagation delays and resolution of the scintillators; the parameters of the model were adjusted to match the resolutions and time slewing effects observed in the real data. With this detector simulation, raw ADC and TDC data are generated, which are processed through the identical analysis chain as the real data.

IV. PARTICLE DISTRIBUTIONS IN SHOWERS

The analysis presented in the following deals with the measurement of the angular distribution of (unidentified) charged particles in air showers, based on tracks reconstructed in the upper drift chamber of the CRT prototype detector module.

A. Particle flux in showers

Averaging over many cascades, the distribution of particles in air showers can be described by the flux f:

$$f_i(E,\mathbf{n}^*,\mathbf{r}^*)=\left\langle \frac{dn_i}{dE\,d\Omega^*\,dA^*} \right\rangle .$$

Here, f gives the average number of shower particles of type i and direction $\mathbf{n}^*$, per energy interval, solid angle, and area, as seen in a detector at a distance $\mathbf{r}^*$ from the shower axis $\mathbf{a}$, with $\mathbf{a}\cdot\mathbf{r}^*=0$. The $*$ indicates that quantities are measured in a local coordinate system, in which the shower axis coincides with the z axis. The area A^* is taken perpendicular to the shower axis. The usual NKG distribution is obtained by integrating over dE and $d\Omega^*$, and by summing over charged particle types. An ideal direction-sensitive detector measures the energy-integrated flux F:

$$F(\mathbf{n}^*,\mathbf{r}^*)=\sum_i \left\langle \frac{dn_i}{d\Omega^*\,dA^*} \right\rangle = \sum_i \int f_i(E,\mathbf{n}^*,\mathbf{r}^*)dE .$$

For a detector such as the CRT module, the actual rate of reconstructed particle tracks is given by a slightly more complicated expression:

$$F_{\rm obs}(\mathbf{n}^*_{\rm obs},\mathbf{r}^*)=\left\langle \frac{dn_{\rm rec}}{d\Omega^* dA^*} \right\rangle$$

$$=\int \epsilon_e(E) f_e(E,\ldots)dE+\int \epsilon_\mu(E) f_\mu \cdots (E,\ldots)dE+\int \epsilon_e(E)\int f_\gamma(E',\ldots)P(E',E)dE'\,dE .$$

Here, $\epsilon(E)$ is the efficiency for track reconstruction. Since the track fit is based on the assumption of a straight trajectory, low momentum tracks with large multiple scattering in the chamber gas will more frequently fail the tracking cuts, resulting in an effective momentum cutoff near 10 MeV/c for electrons. Figure 10 displays the tracking efficiency obtained by a detailed detector simulation. In addition, particles may be absorbed in the material above the drift chamber. The first term in the equation corresponds to the dominant electron (and positron) contribution, and the second term summarizes all other charged particles. Finally, because of the additional material above the active detector volume, photons of energy E' may interact and give rise to electrons of energy E, as described by the third term. While the interaction probability $P(E',E)$ is small, the term is nevertheless significant, as the photon flux is significantly larger than

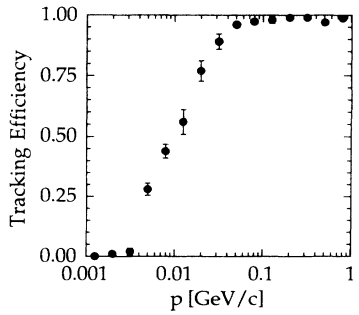

FIG. 10. Probability that an electron track crossing the drift volume is reconstructed and passes the selection criteria, as a function of momentum, derived using a detailed Monte Carlo simulation of the detector.

the electron flux. Finally, we note that the measured direction $\mathbf{n}^*_{\rm obs}$ of a particle may deviate from its true $\mathbf{n}^*$, either due to measurement errors in the tracking, or because the measured shower axis will in general deviate from the true axis due statistical fluctuations in the shower development and due to imperfections in the measuring device, in our case the scintillator array. For our measurements, the angular error of about 1.3° of the air shower array is by far the dominant effect.

We may rewrite this expression for $F_{\rm obs}$ as

$$F_{\rm obs}(\mathbf{n}^*_{\rm obs},\mathbf{r}^*)=\left[\frac{dn_{\rm rec}}{d\Omega^*\,dA^*}\right] \cong \bar{\epsilon}_e\int f_e(E,\ldots)dE+\bar{\epsilon}_\gamma\int f_\gamma(E,\ldots)dE\ ,$$

where we have introduced spectrum-averaged efficiencies $\bar{\epsilon}_e$ and $\bar{\epsilon}_\gamma$. For the typical shower sizes in our sample, and for the rather small core distances of less than 20 m, we expect that over 97% of all charged particles are electrons. We can therefore neglect the small contribution from muons and hadrons. Since the energy spectrum of particles depends on the distance from the shower core and on the angle to the shower axis, the efficiencies vary somewhat with these parameters. From Monte Carlo simulations (with a lower energy cutoff of 4 MeV for shower electrons and photons), we find typical values of $\bar{\epsilon}_e=(65\pm3)\%$ and $\bar{\epsilon}_\gamma=(8\pm2)\%$. The "photon efficiency" $\bar{\epsilon}_\gamma$ can be understood as a convolution of the $\approx 15\%$ interaction probability with the tracking efficiency. Given that the total number of photons (above the 4 MeV cut) is about three times the number of electrons, these efficiencies imply that the observed number of tracks should more or less coincide with the number of charged shower particles, the 35% loss of low-energy electrons being roughly compensated by the $\bar{\epsilon}_\gamma f_\gamma/f_e\approx 8\%\times 3$ tracks generated by photon interactions:

$$F_{\rm obs}(\mathbf{n}^*_{\rm obs},\mathbf{r}^*)\cong\bar{\epsilon}_{\rm eff}\int f_e(E,\ldots)dE\ ,$$

with an average net efficiency of $(88\pm5)\%$. In the following, we will present distributions in terms of $F_{\rm obs}(\mathbf{n}^*_{\rm obs},\mathbf{r}^*)$, obtained by counting tracks weighted with the inverse of the geometrical area A^* over which the track could be detected. We present angular distributions in terms of normalized particle densities, where constant efficiency factors cancel. At the level of precision aimed at in this study—the 10–20% range—efficiency changes start to become significant only at large angles to the shower axis, at about 20°, due to the softening of the energy spectra.

The flux F depends on the type and energy of the primary particle, on the depth in the atmosphere, and on the age of the shower. Because of limited statistics, and since the angular and radial distributions are expected to vary little with depth, we average over those parameters and use just the shower size to characterize a given event. For most of the analysis, we use the data sample with the cuts on shower parameters as described earlier; in particular, we require a fitted shower size $N>30\,000$. The median and average shower sizes in the sample were $45k$ and $50k$, respectively. In total, 5100 showers were used, after all cuts.

B. Hit and track density in the upper drift chamber of the tracking module

For the selected sample of air shower events, on average 8.6 hits were found per wire of the upper drift chamber. From these hits, on average 2.7 straight tracks were reconstructed per event (Fig. 11). As discussed before, a track has to show hits on at least five of the six wires, and a straight-line fit probability in the drift (x-z) view exceeding 2%. In counting tracks, no cuts were applied concerning the pad (y-z) fit; however, for analyses using the pad data a similar probability cut is applied there. About 83% of the tracks had hits on all six wires; 17% were missing one hit. In busy events with more than 30 hits per wire, the fraction of tracks with six hits dropped to about 66%, largely due to the appearance of fake tracks with hits on five wires. In events with less than 10 to 15 tracks, on the other hand, saturation effects and related pattern recognition problems proved to be negligible.

At first glance, it appears surprising that only about 30% of all hits can be associated with straight tracks, in particular since the majority of the extra hits are obviously correlated with shower particles—if the chamber was triggered on single muon tracks, few noise hits besides the single track were observed. Several effects generate extra hits in showers:

(a) A fraction of the genuine electron tracks will exhibit kinks due to multiple scattering and will be rejected by the track quality cuts. The visual inspection of events does indeed frequently show clean but significantly curved tracks.

(b) Tracks may leave the tracking chamber on the side and not have the minimum number of hits required for the reconstruction. In particular, low-momentum electrons are easily scattered towards large angles.

(c) If two or more hits of one track are shared with other tracks, the track will not be reconstructed, leaving unassigned hits.

A full Monte Carlo simulation for the detector, including the effects listed above, predicts that 60% of all hits can be associated with reconstructed tracks, well above the experimental value of 30%. However, this discrepan-

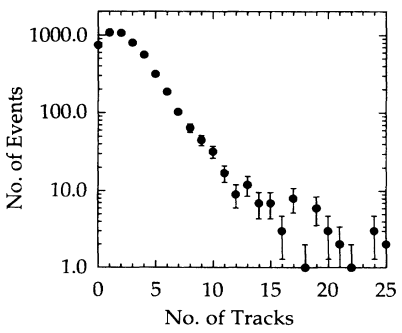

FIG. 11. Distribution in the number of tracks reconstructed in the upper drift chamber of the CRT module, for shower events with shower size above $30k$.

cy is not too surprising, since the majority of the extra hits in the data are most likely caused by very soft electron tracks, with energies below a few MeV. As illustrated in Fig. 10, none of these tracks will be accepted as straight track. With this fact in mind, the Monte Carlo studies use momentum cuts of 2 to 4 MeV in the shower simulation, and of 1 MeV in the detector simulation, in order to limit the total CPU time. As a result, the Monte Carlo estimates should be reliable as far as the number of reconstructed tracks is concerned (since the Monte Carlo cutoff is well below the detector cutoff for track reconstruction), but the total number of hits on the wires of the drift chamber will necessarily be underestimated (since even 100 keV electrons can generate hits on several wires).

A first consistency check on the data from the tracking module is to establish that the module data follow the array data, in particular that the mean number of tracks observed in the module is proportional to the shower size measured in the array, and that the track density decreases with increasing distance from the core as expected for the NKG distribution. Figure 12 shows the mean number of hits per wire of the tracking module as a function of shower size, for different distances to the shower core. Data are indeed consistent with a linear relationship. The corresponding plot for the mean number of tracks as a function of shower size is given in Fig. 13; in this one case only six-hit tracks are used, since for the few events with very large shower sizes and small core distances the number of fake five-hit tracks starts to become significant.

Figure 14 shows the number of hits and the number of tracks as a function of the distance to the shower core, for showers with sizes ranging from 30 000 to 60 000 particles. For easier comparison, the hit and track densities are normalized to the relevant effective area A^* of the tracking module. Also shown are the particle densities measured in the scintillation counters and the densities of charged secondaries above 2 MeV generated by the AIRCAS shower Monte Carlo program. As expected and

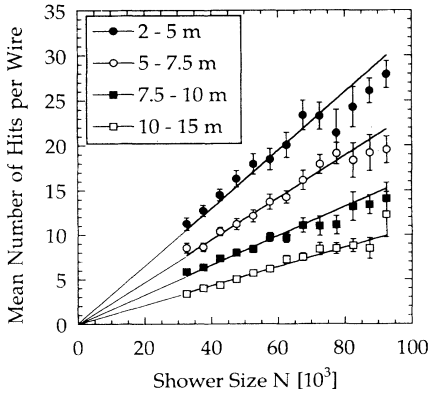

FIG. 12. Mean number of hits $\langle n_{\rm hit} \rangle$ observed per wire of the upper drift chamber of the CRT module, as a function of the shower size N, for different ranges in core distance. The lines represent fits with $\langle n_{\rm hit} \rangle \sim N$.

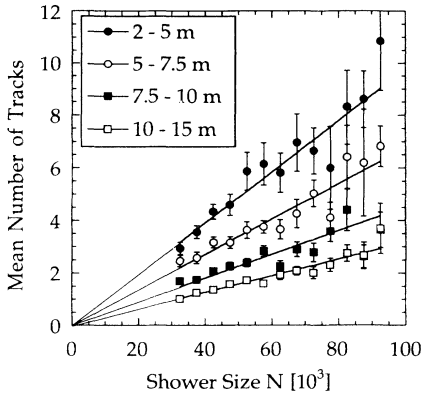

FIG. 13. Mean number of tracks $\langle n_{\rm trk} \rangle$ in the upper drift chamber, as a function of the shower size N, for different ranges in core distance. Only tracks with six wire hits are counted. The lines represent fits with $\langle n_{\rm trk} \rangle \sim N$.

discussed above, the number of tracks per unit area in the tracking module is close to the track density in the scintillators; the hit density is significantly larger. At small distances, the scintillator data fall below the Monte Carlo prediction; the reason is a slight bias introduced by the selection criteria, which reject events where the particle density in a scintillator station close to the core fluctuates upwards beyond 30 particles, but keep events with lower-than-average maximum pulse height.

In summary, we can state that the track densities in the tracking module are quantitatively understood.

C. Angular distributions of particles in showers

Rather than using polar coordinates θ,ϕ to describe the direction of a particle, it is convenient to parametrize its unit vector **n** in terms of the slopes $s_x = dx/dz$,

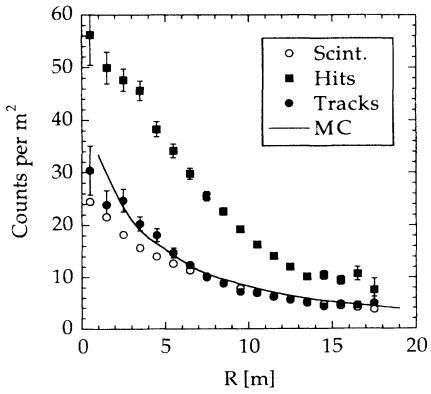

FIG. 14. Mean number of hits per wire and of tracks in the upper drift chamber of the CRT module, as a function of core distance, for shower sizes between $30k$ and $60k$. Both quantities are normalized per unit area. Also shown is the mean number of particles per unit area detected in the counters of the scintillator array. The curve represents the Monte Carlo shower simulation of the number of charged particles per unit area.

$s_y = dy/dz$ of the trajectory:

$$\mathbf{n} = \frac{1}{\sqrt{1+s_x^2+s_y^2}}(s_x, s_y, 1) .$$

Note that in our convention all directional vectors point upward, that is towards the apparent point of origin of a particle. In the detector system, s_x is determined from the drift time information, s_y from the cathode pad data. The transformation between the detector coordinate system and the shower coordinate system (where the shower axis points along z) is straightforward; particle densities have to be multiplied by the appropriate Jacobian.

We will frequently use the following quantities to describe the location and direction of a shower particle (see Fig. 15): the distance $\mathbf{r}^*$ from the shower axis; the angle θ^* between the particle's direction $\mathbf{n}^*$ and the shower axis $\mathbf{a}$, $\cos(\theta^*) = \mathbf{a}\cdot\mathbf{n}^*$; the radial slope s_r^* of the particle's trajectory; and the tangential slope s_ϕ^* of the trajectory. The latter two quantities are best represented in a coordinate system where the first axis (z^*) is defined by the shower direction $\mathbf{a}$, the second (radial) axis by the position vector $\mathbf{r}^*$, and the third (tangential) axis by $\mathbf{a}\times\mathbf{r}^*$. In this system, the particle's direction can be expressed as

$$\mathbf{n} = \frac{1}{\sqrt{1+s_r^{*2}+s_\phi^{*2}}}(s_r^*, s_\phi^*, 1) .$$

Obviously, the flux $F(\mathbf{n}^*, \mathbf{r}^*)$ is invariant under rotations about the shower axis and depends only on the distance $r^* = |\mathbf{r}^*|$, and on the radial and tangential slopes of $\mathbf{n}^*$, s_r^* and s_ϕ^*, with the associated angles $\delta_r^* = \arctan(s_r^*)$ and $\delta_\phi^* = \arctan(s_\phi^*)$.

Shower particles are expected to be collimated around the shower axis. The data demonstrate this feature very clearly. In Fig. 16, the track slopes s_x (in the drift direction of the tracking module) and s_y (in the pad direction) are seen to follow the slopes of the shower axis from the scintillator data.

For a quantitative comparison with Monte Carlo shower models, we plot in Fig. 17 the measured distribution in the angle θ^* between the particle direction and the shower axis, for shower sizes in the range from $30k$ to $100k$ (solid circles). The distribution, which is sharply peaked at $\theta^* = 0$, is normalized to unity over the interval 0 to 20°. Dividing the range of shower sizes into finer bins, we did not see any dependence on the shower size. For comparison, we include results obtained with the AIRCAS generator for a mixture of primary nuclei (p,C,N,O,Fe) in the energy range of a few 10^{14} eV, with a low-energy cutoff of 2 MeV for shower electrons. The generated angular distributions of secondaries (including muons and charged hadrons) turned out to be rather insensitive to details of the composition and to the energy of the primary. The curves in Fig. 17 refer to different Monte Carlo distributions: the dashed line shows the intrinsic distribution of shower particles (with an energy cut of 2 MeV for electrons); the solid line gives the same distribution after the errors in the determination of the shower axis with the scintillator array are taken into account by smearing the Monte Carlo shower axis with a Gaussian of width 1.3° in both the x and y directions. The dotted curve shows the Monte Carlo distribution, after smearing the axis, for particles with at least 10 MeV

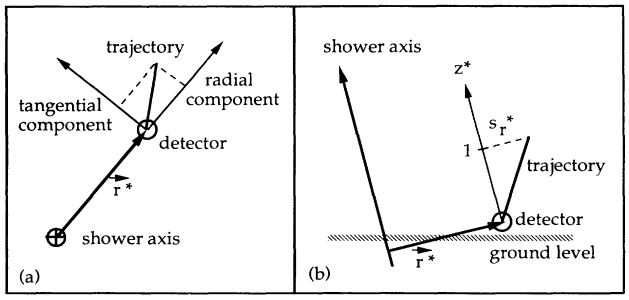

FIG. 15. Definition of coordinate systems, indicating the radial and tangential components of particle vectors: (a) viewed along the shower axis, and (b) viewed from the tangential direction. By definition, both the shower axis ($=z^*$ axis) and the particle trajectory are considered to point upward, i.e., to the point of origin of a particle.

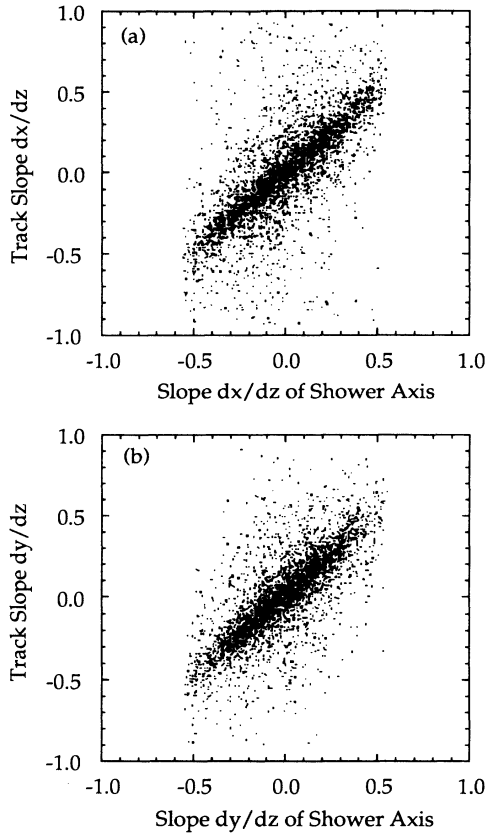

FIG. 16. Distribution of the measured track slopes in x (=drift direction) and y (=wire direction), relative to the corresponding slopes of the shower axis as determined from the scintillator array, and transformed to the CRT module coordinate system.

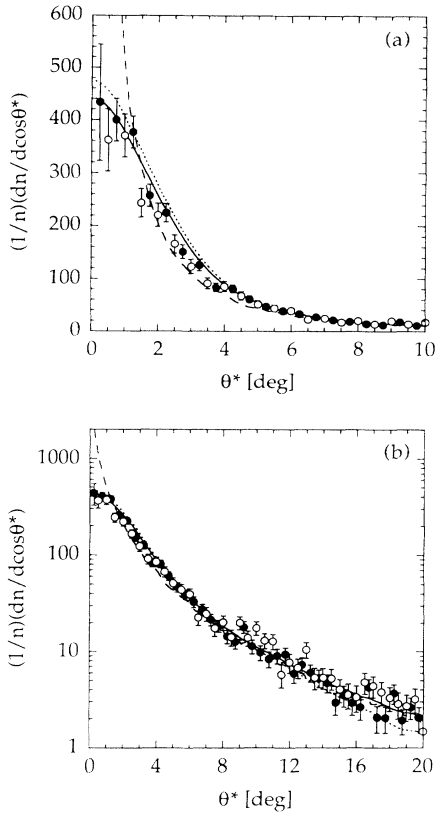

FIG. 17. Distribution $(1/n)(dn/d\cos\theta^*)$ in the angle θ^* between particle tracks and shower axis, normalized to 1 for the interval 0° to 20°, (a) on linear scale, and (b) on logarithmic scale, for tracks at medium distance from the shower axis (5 m $\leq r \leq$ 12 m, with $\langle r \rangle \approx 8$ m). Solid circles represent data points; open circles show the results of a full Monte Carlo simulation of the air shower and of the detector module, using the AIRCAS and GEANT codes, respectively. The lines represent the particle distributions in Monte Carlo air showers, before detector simulation. Dashed: distribution of shower particles above 2 MeV energy; solid: same, after smearing with the 1.3° measurement accuracy for the shower axis; dotted: including smearing of the axis and a 10 MeV energy cutoff.

energy, to simulate the effect of the tracking cutoff; we see that the cut causes only a small change of the slope in the tail of the distribution at large angles [Fig. 17(b)]. Finally, the open points represent a full Monte Carlo simulation of the detector, of its response, and of the pattern recognition and track reconstruction. Above angles of a few degrees, the detector provides a reliable measurement of the intrinsic angular distributions; at smaller angles, the measurement is dominated by the limited precision of the reconstruction of the shower axis in the scintillator array. Once this measurement error is taken into account, the Monte Carlo distributions with and without CRT detector effects agree with each other. Therefore, we include in the following figures only the Monte Carlo curves representing the distributions of charged shower particles at the generator level, with angles smeared by 1.3°. Generally, the curves shown are based on the AIRCAS Monte Carlo program. For the distributions discussed in this work, fluxes obtained using the CORSIKA Monte Carlo program did not show significant differences to AIRCAS.

To characterize the width of this angular distribution, we use its median value (in the interval 0° to 20°). Figure 18 displays the median angle as a function of the distance from the shower axis. As expected, the width of the angular distribution increases with the distance from the shower core. We find good agreement between simulation and measurement.

Looking at the angular distributions in more detail, one expects to see a different behavior in the distributions of radial and of tangential angles of trajectories [16] (see Fig. 15)]: the distribution in the tangential angle δ_ϕ^* is obviously symmetric for positive and negative values of δ_ϕ^*. The distribution in the radial angle δ_r^*, however, should show particles at larger r^* pointing towards the shower axis as their point of origin, which implies a preference for negative values of δ_r^*. The distribution of tracks in δ_r^* and δ_ϕ^* is plotted in Fig. 19, for tracks at medium distances (5 to 12 m) from the shower axis. The strong collimation around the shower axis is again obvious, and an asymmetry of the distribution in the radial direction is visible. For a more quantitative study, we use the projections of this distribution onto the radial and tangential directions. The resulting radial and tangential angular distributions for tracks are presented in Fig. 20. The distribution of tangential track slopes is symmetric about 0; the distribution of radial slopes is clearly biased towards negative slopes. This trend can be characterized by plotting the median of the track angular distribution (Fig. 21). Equivalent results are obtained using the mean values. The median radial track angle varies linearly with the distance from the core, at a rate of $-0.15 \pm 0.01(\text{stat}) \pm 0.03(\text{syst})°/\text{m}$. This means that (on average) the particles point towards a source on the shower axis at a height of about 400 m above ground. This value is consistent with the intuitive expectation,

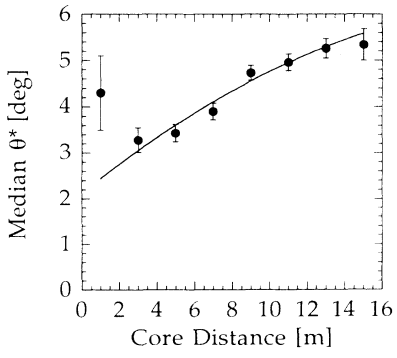

FIG. 18. Median angle between tracks and the shower axis (for the interval 0° to 20°), as a function of the distance to the shower core. The curve represents the Monte Carlo result for shower particles, taking into account the smearing of the shower axis.

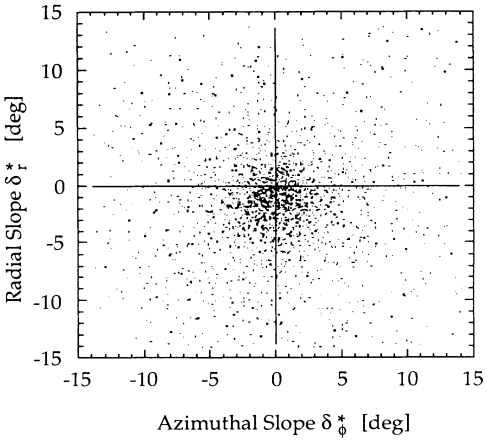

FIG. 19. Distribution of track angles $\delta_r^* = \arctan(s_r^*)$ and $\delta_\phi^* = \arctan(s_\phi^*)$ in the tangential and radial directions, respectively. The angles are defined relative to the shower axis from the scintillator array (see Fig. 15).

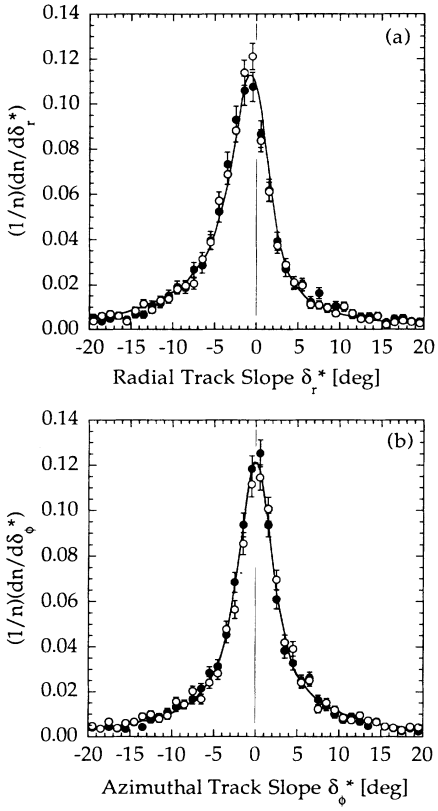

FIG. 20. Distribution of the radial (a) and tangential (b) track slopes for tracks at medium distances from the shower core ($5\ \text{m} \le r \le 12$ m, with $\langle r \rangle \approx 8$ m). Open data points represent the tracks reconstructed using both drift time and cathode pad information. Solid data points are obtained using only the drift time information, and selecting showers with appropriate core locations (see text). All distributions are normalized to unit area. Lines: Monte Carlo results for shower particles, taking into account the smearing of the shower axis.

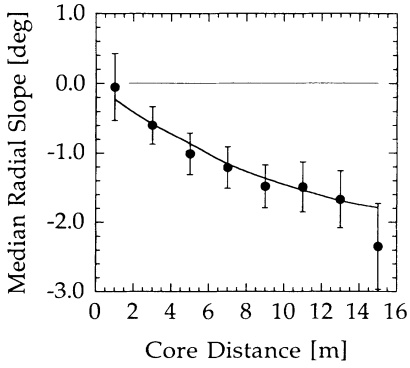

FIG. 21. Median values of the radial track distributions (over the angular range $-20°$ to $+20°$), as a function of the distance to the shower core. Line: shower Monte Carlo result.

namely that the radiation length of air of about 300 m sets the relevant scale. The transverse spread of a shower will be determined by the last generation of secondaries—those produced in the last one or two radiation lengths above ground—since these particles have the lowest energies and hence the largest multiple scattering angles.

For the measurement of these angular distributions, it is crucial that there is no systematic error in the determination of the shower axis. Since the CRT module is located almost at the center of the array, a systematic inward or outward tilt of showers with cores near the periphery of the array could shift the median track angles. As discussed in detail above, we verified that such effects do not exceed 0.5°.

One can furthermore check the symmetry of the distributions under rotations about the shower axis. Again, we found no evidence for systematic effects. As a final check, we note that there are two ways to measure the angular distributions $F(\mathbf{n}^*, \mathbf{r}^*)$ of particles in air showers from these data of the CRT module. One can reconstruct tracks in space using both the drift time information and the cathode pad data, and then take the projections onto the appropriate radial or tangential directions in the local shower coordinate frame. Alternatively, one can reconstruct track projections in the x-z projection (of the CRT module coordinate system) using the drift time information only, and compare these slopes with the corresponding projection of the shower axis. The radial (s_r^*) or tangential (s_ϕ^*) slopes of particle directions can then be measured by selecting events with the appropriate relative orientation of the drift direction and the vector from the shower core to the module position. This second approach has the advantage that only the relatively simple wire signals are used, avoiding the complex analysis of cathode pad data, which are more prone to multitrack overlap problems because of their longer shaping times. Both methods were used; to measure tangential and radial distributions based on the drift information only, events with angles between drift direction and vector to the shower core of $-30°$ to $+30°$ and of 60° to 120° were

selected, respectively. As demonstrated in Fig. 20, the agreement between the two techniques is very good.

The non-Gaussian shape of the angular distributions can be traced to the fact that the measured angular distributions represent a superposition of particles of different energies, with an energy-dependent angular distribution; deviations from the shower axis due to multiple scattering will scale as the inverse of the momentum of a particle. The non-Gaussian shape also implies that the angular distributions cannot be parametrized as $F_r(\delta_r^*)F_\phi(\delta_\phi^*)$; particles with large δ_r^* have a wider distribution in δ_ϕ^*, and vice versa (Fig. 22). At large angles, data and Monte Carlo results in Fig. 22 start to deviate slightly; this is not unexpected since here the mean particle energies become quite small, and the effect of the 10 MeV tracking cutoff should begin to be visible. Indeed, the agreement improves if only shower particles above 10 MeV energy are plotted (dashed curves).

D. Two-track correlations

For tracks close to the shower axis, the study of angular distributions of particles is limited by the angular resolution of the array. It is therefore interesting to look at two-track correlations, such as the distribution in the opening angle between pairs of tracks, where the knowledge of the shower axis is not required. This distribution should be sharply peaked at zero opening angle, limited only by the angular resolution of the drift chamber (about 0.6° for the opening angle of two tracks in space), and possibly by effects of multiple scattering in the material above the active volume. Monte Carlo simulations show that the effects of multiple scattering in this distribution (as well as in the other angular distributions shown previously) are negligible. At first, this may seem surprising, given that most particles are rather soft. On the other hand, however, the additional material essentially adds another 0.3 radiation lengths to the ≈30 radiation length of air already above the detector, and it is known that the shapes of particle spectra deep in a shower vary only logarithmically with depth. Angular distributions of shower particles are so stable since particles in the sharply peaked region near the shower axis have high energies and are less influenced by scattering; in the tails, where soft particles dominate, the distributions vary slowly and the redistribution due to scattering is hardly noticed.

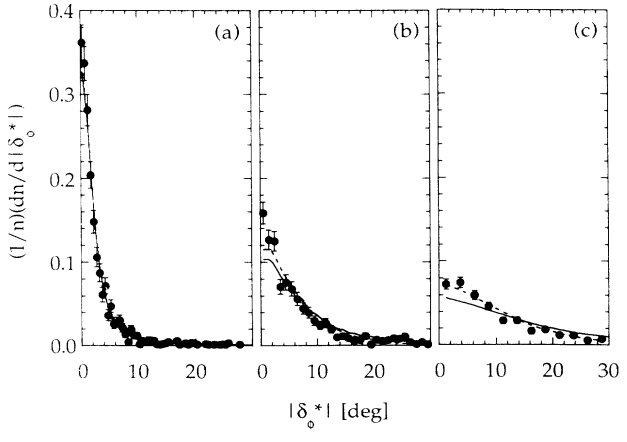

FIG. 22. Distribution in the tangential track slopes δ_ϕ^*, for different ranges in the radial track slopes δ_r^*: (a) $0<|\delta_r^*|<2°$, (b) $5°<|\delta_r^*|<10°$, (c) $10°<|\delta_r^*|<30°$. The distributions are normalized to unit area. Solid lines: shower Monte Carlo result for 2 MeV cutoff, including smearing of the shower axis; dashed lines: for 10 MeV cutoff.

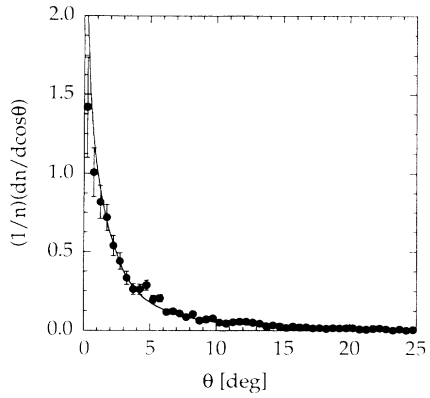

FIG. 23. Distribution in the opening angle in space between pairs of tracks reconstructed in the CRT module. The distribution is normalized to unit area. Line: Monte Carlo result for shower particles.

The distribution in the opening angle is presented in Fig. 23, based on showers with sizes in the $30k$ to $100k$ range, and using the standard track definitions. Included are Monte Carlo results, which reproduce well the sharp peaking at zero opening angle. The lowest data point (covering the range 0°–0.5°) falls slightly below the Monte Carlo curve, possibly indicative of the resolution of the tracking system. However, statistics are too small for quantitative conclusions.

V. SUMMARY AND OUTLOOK

Using a tracking detector, we have measured the angular distribution of charged particles in extensive air showers. The particle distributions are sharply peaked around the shower axis, with a tendency to point towards a source on the shower axis. In all variables studied, we find rather good agreement between the Monte Carlo generated distributions of shower particles, and the corresponding distributions of tracks reconstructed in the CRT module (after accounting for the smearing of the shower direction measured in the scintillator array). Small deviations at the 20% level, such as seen in Fig. 22, are within the range of detector effects; after all, the detector effectively substitutes some converted photon tracks for lost low-energy electron tracks. We should point out, however, that the present experiment is not sensitive to the detailed shape of the distributions very close to the shower axis (within 1° to 2°).

We conclude that the angular distributions of charged particles in hadronic showers are reliably predicted by

shower Monte Carlo codes such as AIRCAS or CORSIKA. Based on these Monte Carlo codes, we expect that tracking arrays will reconstruct showers axes with errors in the range of $2°-3°/\sqrt{n}$, where n is the number of detected tracks [8]. Preliminary results for multitrack events in the prototype module are consistent with the Monte Carlo estimates, but the number of events with many fully reconstructed tracks is too small to draw definite conclusions. Details will be reported once the superior data from several full-scale modules now under test are available.

With a trigger threshold of 50 tracks, and a mean number of about 100 tracks per event, an array of CRT detectors as proposed in [8] should reach $0.2°-0.3°$ resolution in the TeV energy range.

ACKNOWLEDGMENTS

We would like to thank C. Dreher and Dr. J. Spitzer and Dr. B. Schmidt for their contributions in early stages of the experiment, as well as Dr. K. Bernlöhr for numerous comments and suggestions on the manuscript.

[1] M. Samorski and W. Stamm, Astrophys. J. **268**, L17 (1983).
[2] T. Weeks *et al.*, Astrophys. J. **342**, 379 (1989).
[3] A. Adam *et al.*, Proposal for the GRANDE facility, GRANDE 90-005, 1990 (unpublished).
[4] J. A. Goodman, in *High Energy Gamma-Ray Astronomy,* Proceedings of the Conference on High Energy Gamma-Ray Astronomy, Ann Arbor, Michigan, 1990, edited by J. Matthews, AIP Conf. Proc. No. 220 (AIP, New York, 1990), p. 275.
[5] A. Karle, in *High Energy Gamma-Ray Astronomy* [4], p. 305.
[6] G. Appolinari *et al.*, Nucl. Instrum. Methods **A263**, 255 (1988).
[7] J. Poirier *et al.*, Nucl. Instrum. Methods **A264**, 81 (1988).
[8] J. Heintze *et al.*, Nucl. Instrum. Methods **A277**, 29 (1989).
[9] M. Feuerstack *et al.*, Nucl. Instrum. Methods **A310**, 287 (1991); M. Panter *et al., ibid.* (to be published).
[10] ALEPH Collaboration, D. Decamp *et al.*, Nucl. Instrum. Methods **A294**, 121 (1990); **A303**, 393 (1991).
[11] H. Aihara *et al.*, IEEE **NS-30**, 76 (1983); D. Vilanova *et al.*, Nucl. Instrum. Methods **A235**, 285 (1985); S. R. Amendolia *et al., ibid.* **217**, 317 (1983).
[12] R. Brun *et al.*, CERN Report No. DD/EE/84-1 (unpublished).
[13] K. Greisen, Annu. Rev. Nucl. Sci. **10**, 63 (1960).
[14] J. N. Chapdevielle *et al.*, KfK Report No. 4998, 1992 (unpublished).
[15] J. Spitzer, Physikalisches Institut der Universität Heidelberg Report No. HD-PY-92/08, 1992 (unpublished).
[16] A. M. Hillas, J. Phys. G **8**, 1461 (1982).

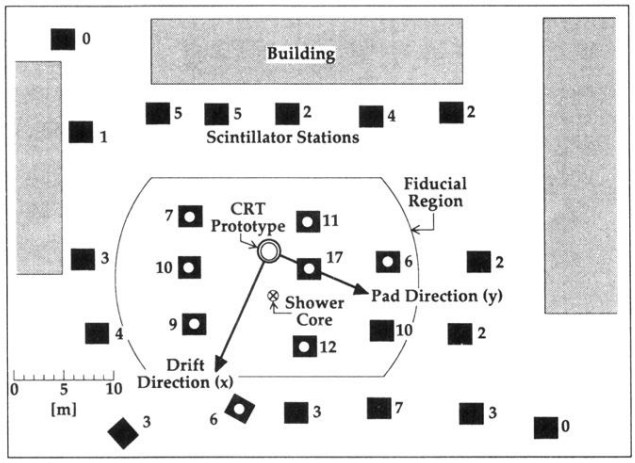

FIG. 1. Air shower array operated at the Max Planck Institut für Kernphysik. The 25 stations contain scintillators with 0.8 m^2 active area. The stations marked with a white dot provide the trigger for the array. Shower cores are accepted within the indicated fiducial region. The numbers show the pulse heights (in units of particles) for a typical shower with its core indicated near the center of the array. Also shown is the location of the half-scale CRT prototype module, and the orientation of the drift chambers inside the module.

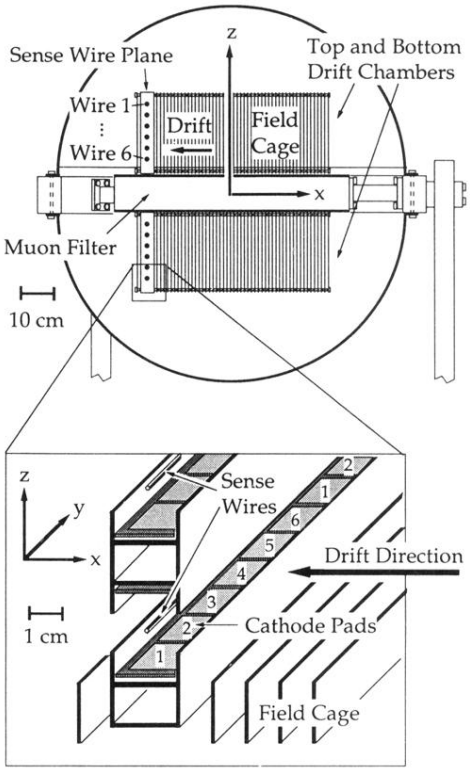

FIG. 2. Illustration of the half-scale prototype module, showing the two drift chambers with their field cages and sense wire planes, the iron muon filter, and the vessel consisting of the aluminum support ring and two aluminum half-spheres. The support ring also contains all feedthroughs for supply voltages and signal cables. The lower figure gives details of the construction of the wire chamber, where aluminum profiles are used to define the gas amplification cells. Printed circuit boards in the profiles provide the cathode pads for the determination of the coordinate along the wire. The pads are read out through traces on the back of the board; every sixth pad in a row is connected to the same electronics channel.